Cyclic muscle contractions reinforce the acto-myosin motors and mediate the full elongation of *C. elegans* embryo

Anna Dai[1] **and Martine Ben Amar**[1*]

***For correspondence:**
martine.benamar@phys.ens.fr (MBA)

[1]Laboratoire de Physique de l'Ecole normale supérieure, ENS, Université PSL, CNRS, Sorbonne Université, Université Paris Cité, F-75005 Paris, France

Abstract The paramount importance of mechanical forces in morphogenesis and embryogenesis is widely recognized, but understanding the mechanism at the cellular and molecular level remains challenging. Because of its simple internal organization, Caenorhabditis elegans is a rewarding system of study. As demonstrated experimentally, after an initial period of steady elongation driven by the actomyosin network, muscle contractions operate a quasi-periodic sequence of bending, rotation and torsion, that leads to the final 4-fold size of the embryo before hatching. How actomyosin and muscles contribute to embryonic elongation is investigated here theoretically. A filamentary elastic model that converts stimuli generated by biochemical signals in the tissue into driving forces, explains embryonic deformation under actin bundles and muscle activity, and dictates mechanisms of late elongation based on the effects of energy conversion and dissipation. We quantify this dynamic transformation by stretches applied to a cylindrical structure that mimics the body shape in finite elasticity, obtaining good agreement and understanding for both wild-type and mutant embryos at all stages.

Introduction

Mechanical stresses play a critical role during embryogenesis, affecting complex biological tissues such as the skin, the brain, and the interior of organs. There are many studies in recent decades, for example, the pattern of the intestine (***Coulombre and Coulombre*** (***1958***); ***Hannezo et al.*** (***2011***); ***Li et al.*** (***2011***); ***Ben Amar and Jia*** (***2013***); ***Shyer et al.*** (***2013***)), the brain cortex (***Toro and Burnod*** (***2005***); ***Goriely et al.*** (***2015***); ***Ben Amar and Bordner*** (***2017***); ***Tallinen et al.*** (***2016***)), and the circumvolutions of the fingerprints (***Kücken and Newell*** (***2005***); ***Ciarletta and Ben Amar*** (***2012***)), which have been interpreted as the result of compressive stresses generated by the growth that occurs a few months after fertilization in humans. The superposition of mechanical stresses, cellular processes (e.g., division, migration), and tissue organization is often too complex to identify and quantify. For example, independent of growth, stresses can be generated by different molecular motors, among which myosin II, linked to actin filaments, is the most abundant during epithelial cell morphogenesis (***Vicente-Manzanares et al.*** (***2009***)) and cell motility (***Cowan and Hyman*** (***2007***); ***Olson and Sahai*** (***2009***); ***Palumbo et al.*** (***2022***)). Spatial distribution and dynamics of myosin II strongly influence the morphogenetic process (***Levayer and Lecuit*** (***2012***); ***Lv et al.*** (***2022***)), as demonstrated for Drosophila (***Bertet et al.*** (***2004***); ***Blankenship et al.*** (***2006***); ***Saxena et al.*** (***2014***); ***Shindo and Wallingford*** (***2014***)) and also for *C. elegans* embryos (***Priess and Hirsh*** (***1986***); ***Gally et al.*** (***2009***); ***Ben***

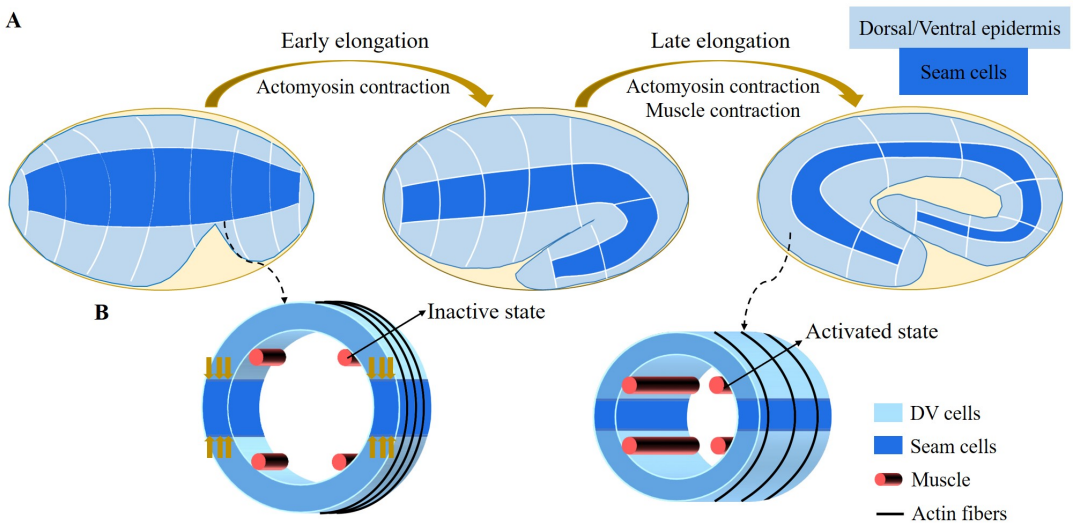

Figure 1. (A) Overview of *C. elegans* embryonic development. Three epidermal cell types are found around the circumference: dorsal, ventral and seam cells. (B) Schemes showing a *C. elegans* crossn section of the embryo. Small yellow arrows in the left image indicate the contraction force that occurred in the seam cell. Four muscle bands under the epidermis and actin bundles surround the outer epidermis.

Amar et al. (***2018***)).

Embryonic elongation of C. elegans before hatching provides an attractive model of matter reorganization in the absence of growth. It occurs after ventral enclosure and takes about 240 minutes to transform the lima bean-shaped embryo into the final elongated worm form: the embryo elongates four times along the anterior/posterior axis by (***McKeown et al.*** (***1998***)). The short lifespan of the egg before hatching and its transparency make this system ideal for studying the forces that exist at or near the cortical epithelium . However, in contrast to Drosophila and zebrafish embryonic development, there is no cell migration, cell division, or significant change in embryonic volume (***Sulston et al.*** (***1983***); ***Priess and Hirsh*** (***1986***)), only remarkable epidermal elongation drives the entire morphogenetic process of *C. elegans* in the post-enclosure period. There are two experimentally identified driving forces for the elongation: the actomyosin contractility in the seam cells of the epidermis, which appears to persist throughout the whole elongation process, and the muscle activity beneath the epidermis, which begins after the $1.7 \sim 1.8$-fold stage. The transition is well defined, because the muscle involvement makes the embryo rather motile, and any physical experiments such as laser fracture ablation of the epidermis, which could be performed and achieved in the first period (***Vuong-Brender et al.*** (***2017a***)), become difficult. Consequently, the elongation process of *C. elegans* could be divided into two stages: the early elongation and the late elongation, depending on the muscle activation, and Fig.1(A) shows the whole elongation process (***Vuong-Brender et al.*** (***2017a***)). Previously, the role of the actomyosin network in the seam cells during the *C. elegans* early elongation was investigated (***Ben Amar et al.*** (***2018***)). Based on the geometry of a hollow cylinder composed of dorsal, ventral and seam cells, a model including the pre-stress responsible for the enclosure, the active compressive ortho-radial stress combined with the passive stress quantitatively predicts the elongation, but only up to $\sim 70\%$ of the initial length.

For the late elongation phase, the actomyosin network and the muscles together drive the full elongation during this phase (***Vuong-Brender et al.*** (***2017a***)). The muscles play an important role and mutants with muscle defects are unable to complete the elongation process, even though the actomyosin network functions normally (***Lardennois et al.*** (***2019***)). Fig.1(B) shows a schematic image of the *C. elegans* body (***Zhang et al.*** (***2011***)) with four rows of muscles, two of which are under the dorsal epidermis and the other two are under the ventral epidermis. As observed *in vivo*, *C. elegans*

exhibits systematic rotations accompanying each contraction (***Yang*** (***2017***); ***Yang Xinyi et al.*** (***2023***)), and deformations such as bending and twisting. Eventually, the *C. elegans* embryo will undergo an elongation of 1.8-fold to 4-fold. As the activated muscle contracts on one side, the contractile forces are transmitted to the epidermis on that side. Since striated muscles can only perform cycles of contraction and relaxation, their action will tend to reduce the length of the embryo. Therefore, it is necessary to understand how the embryo elongates during each contraction and how the muscle contractions are coupled to the actomyosin activity. This work aims to answer this paradox within the framework of finite elasticity without invoking cellular plasticity and stochasticity, which cannot be considered as driving forces. In addition, several important questions remain unanswered at the late stage of elongation. First of all, we may also observe a torsion of the embryo, but if the muscle activity suggests a bending, this alone cannot explain alone a substantial torsion. Second, a small deviation of the muscle axis (***Moerman and Williams*** (***2006***)) is responsible for a number of rotations, how to relate these rotations to the muscle activation (***Yang*** (***2017***)). Since any measurement on a motile embryo at this scale is difficult, it is useful to explore the mechanism of late elongation theoretically. Furthermore, muscle contraction is crucial for both biological development and activities and has been extensively studied by researchers (***Tan and De Vita*** (***2015***); ***De Vita et al.*** (***2017***)), but how it works at small scales remains to be understood.

Using a finite elasticity model and assuming that the embryonic body shape is cylindrical, we can evaluate the geometric bending deformation and the energy released during each muscle contraction on one side since after each contraction, the muscles relax and then the muscles on the opposite side undergo a new contraction. This cyclic process results in a tiny elongation of the cylinder along its axis of symmetry with each contraction. Each of these contractions correlates with the rotational movements of the embryo (***Yang*** (***2017***)). By repeating these pairs of contractions more than two hundred times, a cumulative extension is achieved, but it must be reduced by friction mechanisms, also evaluated by the model. Furthermore, the mechanical model explains the existence of a torque acting on the position of the head or tail by the coupling of the muscle contraction with the orthoradial actomyosin forces. Finally, the small deviation between the muscles and the central axis experimentally detected (***Moerman and Williams*** (***2006***)) induces cyclic rotations and possibly torsions leading to fluid viscous flow inside the egg. The quantification of all these processes allows the evaluation of physical quantities of the embryo, such as the shear modulus of each component, the interstitial fluid viscosity and the active forces exerted by the actomyosin network and the muscles, which are poorly y known in the embryonic stages.

Our mechanical model accounts for the dynamic deformations induced by the internal stimuli of a layered soft cylinder, allowing us to make accurate quantitative predictions about the active networks of the embryo. Furthermore, our model accounts for the dissipation that occurs in the late period just before the embryo hatches. Our results are consistent with observations of actomyosin and muscle activity (***Vuong-Brender et al.*** (***2017a***); ***Ben Amar et al.*** (***2018***); ***Lardennois et al.*** (***2019***)). The architecture of our work is illustrated in Fig.2.

Results

It is widely recognized that *C. elegans* is a well-established model organism in the field of developmental biology. However, it is less well known that its internal striated muscles share similarities with vertebrate skeletal muscles in terms of both function and structure (***Lesanpezeshki et al.*** (***2021***)). Since they are contractile, the role of the four axial muscles (as shown in Fig.1) in the final shaping of the embryo is almost counterintuitive. In this section, we aim to elucidate the action of these muscles when coupled to the actomyosin network, using a purely mechanical approach. To achieve a quantitative understanding, our method requires a detailed description of the deformation geometry of the embryo, where the body shape is represented by a fully heterogeneous cylinder.

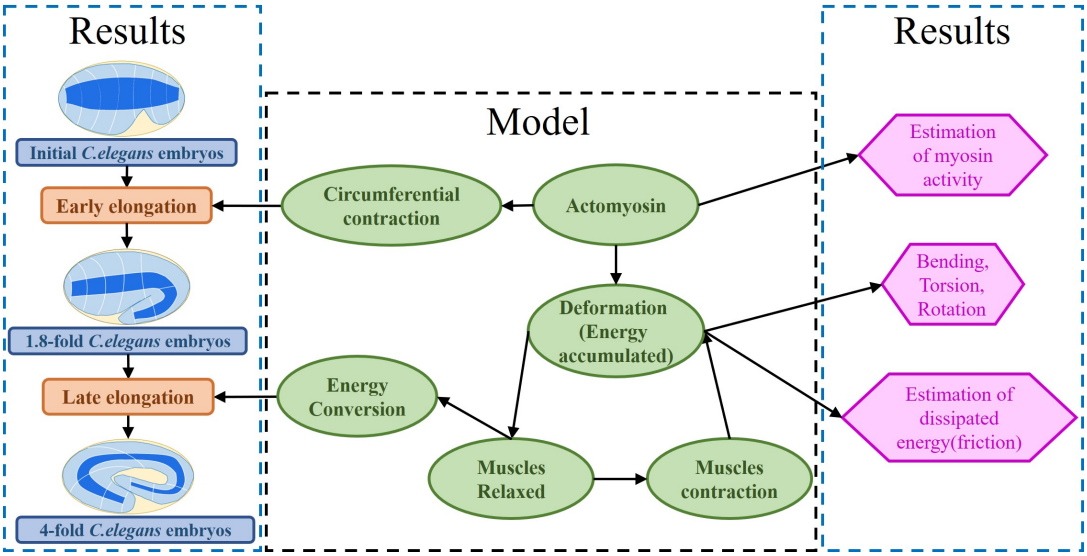

Figure 2. Architecture of the program. The program reflects the framework of the research. On the one hand, the proposed model explains the early and late elongation of the *C. elegans*, on the other hand, the early myosin activity is estimated, the deformations (bending, twisting, rotation) occurring in the late period are recovered, and the estimation of the energy dissipated during muscle activity is achieved.

Geometric and strain deformations of the embryo

The early elongation of the *C. elegans* embryo has been previously studied, which is characterized by an inner cylinder surrounded by epithelial cells located in the cortical position (***Ben Amar et al.*** (***2018***)). The cortex is composed of three distinct cell types - the seam, dorsal, and ventral cells - that exhibit a unique cytoskeletal organization and actin network configuration. Among these, only the seam cells possess active myosin motors that function in the ortho-radial direction, allowing for the circumferential contraction and thereby triggering the early elongation process. In this study, we simplify the cylindrical geometry of the body and treat the epidermis as a unified whole with effective activity localized along the circumference, supported by four muscles distributed beneath the epidermis. The muscles do not play a role in the early elongation phase and have therefore not been considered previously (***Vuong-Brender et al.*** (***2017a***); ***Ben Amar et al.*** (***2018***)). After this period of approximately a 1.8-fold increase in length, muscles parallel to the main axis and actin bundles organized along the circumference will cooperate to drive further elongation. Table. 1 provides the size parameters of *C. elegans* that will be used hereafter.

Table 1. Adopted real size parameters of the *C. elegans* (***Vuong-Brender et al.*** (***2017a***); ***Ben Amar et al.*** (***2018***)).

	Initial	1.8-fold
Radius	11.1 μm	8.2 μm
Length	50 μm	90 μm

We focus on the total deformation of a full cylinder or a thin rod with a length L greater than the radius R and a central vertical axis along the Z direction. Contrary to previous works (***Ciarletta et al.*** (***2009***); ***Ben Amar et al.*** (***2018***)), here we decide to simplify the geometrical aspect due to the mechanical complexity. The biological activity induced by the actomyosin network and muscles is represented by active strains, and the global shape is the result of the coupling between elastic and active strains, modulated by dissipation. Active strains are generated by non-mechanical processes (e.g., biochemical processes): myosin motors and striated muscles derive their energy from ATP hydrolysis, which is converted into mechanical fiber contractions. Due to the significant de-

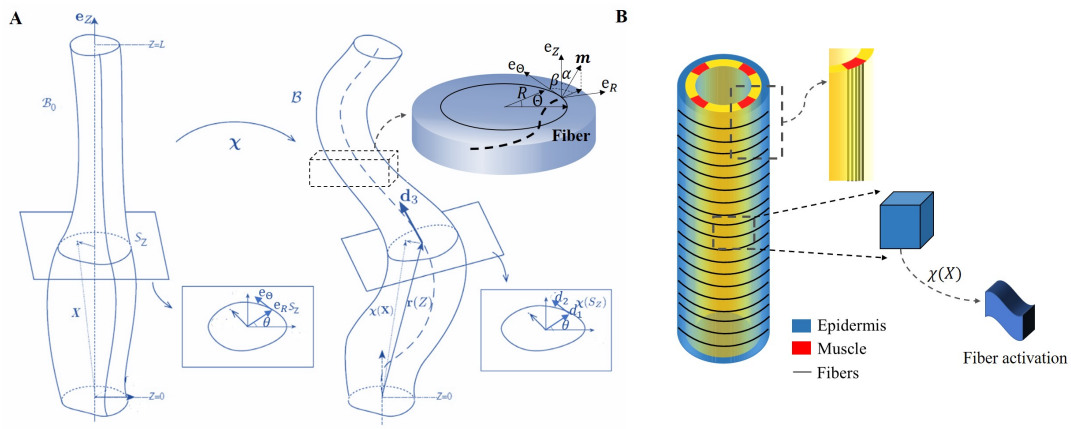

Figure 3. (A) Cylindrical structure in the reference configuration (left) with a vertical centerline and its deformation in the current configuration (right). The deformed configuration is fully parameterized by the centerline $\mathbf{r}(Z)$ (resulting from the distortion of the central axis) and the deformation of each cross section. (B) Schematic representation of the body shape of the *C. elegans* embryo with the cortical epidermis and the four muscles. The fibers are embedded in the cortex. The blue part representing the epidermis shows the outer distribution of the actin organized in horizontal hoop bundles when the muscles are not activated. The yellow part includes the vertical red muscles, represented by axial fibers.

formation observed, the central line is distorted and becomes a curve in three-dimensional space, represented by a vector $\mathbf{r}(\mathbf{Z})$, as depicted in Fig.3(A). Along this curve, perpendicular planar sections of the embryo can be defined, and the deformation in each section can be quantified since the circular geometry is lost with the contractions (***Kaczmarski et al.*** (***2022***)). The geometric mapping is as follows:

$$\chi(\mathbf{X}) = \mathbf{r}(Z) + \sum_{i=1}^{3} \varepsilon a_i(\varepsilon R, \Theta, Z)\, \mathbf{d}_i(Z), \tag{1}$$

where the a_i represents the deformation in each direction of the section with $a_i(0, \Theta, Z) = 0$ so that the Z-axis is mapped to the centerline $\mathbf{r}(Z)$. The small quantity ε is the ratio between the radius R and the length L of the cylinder. The axial extension ζ is given by $\mathbf{r}'(Z) = \zeta \mathbf{d}_3$, where $'$ denotes the first derivative with respect to the material coordinate Z. From the director basis, the Darboux curvature vector reads: $\mathbf{u} = u_1\mathbf{d}_1 + u_2\mathbf{d}_2 + u_3\mathbf{d}_3$, this vector gives the evolution of the director basis along the filamentary line as: $\mathbf{d}_i{}'(Z) = \zeta \mathbf{u} \times \mathbf{d}_i$, see Fig.3(A). Based on the model proposed by B. Kaczmarki *et al*. (***Kaczmarski et al.*** (***2022***)), we define the initial configuration $\mathcal{B}_0$ with material points (R, Θ, Z), and the mapping function $\chi(\mathbf{X})$ connects the initial configuration $\mathcal{B}_0$ to the current configuration $\mathcal{B}$. The geometric deformation gradient is $\mathbf{F} = \mathrm{Grad}\chi = \mathbf{F_e}\mathbf{G}$ (***Nardinocchi and Teresi*** (***2007***)), where $\mathbf{G}$ is the active strain generated by the actomyosin or the muscles, and $\mathbf{F_e}$ is the elastic strain tensor.

Because of the two stages through which the *C. elegans* elongates, we need to evaluate the influence of the *C. elegans* actin network during the early elongation before studying the deformation at the late stage. Thus, the deformation gradient can be decomposed into: $\mathbf{F} = \mathbf{F}_e\mathbf{G}_1\mathbf{G}_0$ (***Goriely and Ben Amar*** (***2007***)) where $\mathbf{G}_0$ refers to the pre-strain of the early period and $\mathbf{G}_1$ is the muscle supplementary active strain in the late period. Actin is distributed in a circular pattern in the outer epidermis, see Fig.3(B), so the finite strain $\mathbf{G}_0$ is defined as $\mathbf{G}_0 = Diag\left(1, g_0(t), 1\right)$, where $0 < g_0 < 1$ is the time-dependent decreasing eigenvalue, operating in the actin zone and is equal to unity in the other parts: $g_0(0) = 1$. In the case without pre-strain, $\mathbf{G}_0 = \mathbf{I}$. The deformation gradient follows the description of Eq.(1) :$\mathbf{F} = F_{ij}\mathbf{d}_i \otimes \mathbf{e}_j, where\ i \in \{1,2,3\}$ and $j \in \{R, \Theta, Z\}$.

Considering a filamentary structure Fig.3(B) with different fiber directions $\mathbf{m}$, these directions are specified by two angles α and β, as outlined in (***Holzapfel*** (***2000***)): $\mathbf{m} = \sin\alpha\sin\beta\,\mathbf{e_R} + \sin\alpha\cos\beta\,\mathbf{e_\Theta} +$

$\cos\alpha\,\mathbf{e_Z},\ \alpha,\beta \in \left[-\pi/2, \pi/2\right]$. For muscle fibers, $\alpha_m = 0$ and $\beta_m = 0$, while for hoop fibers in the actin network, $\alpha_a = \pi/2$ and $\beta_a = 0$. When the muscles are activated and bend the embryo, the actin fibers are tilted with a tilt α, such that $-\pi/2 < \alpha_a < \pi/2$, $\alpha_a \neq 0$, and $\beta_a = 0$. Each active strain is represented by a tensor $\mathbf{G_i} = \mathbf{I} + \varepsilon \mathbf{g_i} \mathbf{m_i} \otimes \mathbf{m_i}$, where g_i represents the activity (g_m for muscles and g_a for actomyosin), and since both are contractile, their incremental activities are negative. Additional calculation details are provided in Section Methods and Materials.

To relate the deformations to the active forces induced by the muscles and the actomyosin network, we assume that the embryo can be represented by the simplest nonlinear hyperelastic model, called Neo-Hookean, with a strain energy density given by $W\left(\mathbf{F}_e\right) = \frac{\mu}{2}\left(tr\left(\mathbf{F}_e \mathbf{F}_e{}^T\right) - 3\right)$. In cylindrical coordinates, the total energy of the system and the associated energy density is:

$$\begin{aligned} \mathcal{W} =& \varepsilon^2 \int_0^L \mathrm{d}Z \int_S V(\mathbf{F}_e, \mathbf{G}) R \,\mathrm{dR}\,\mathrm{d}\Theta, \\ V =& W(\mathbf{F_e}) - p(J-1). \end{aligned} \tag{2}$$

where $J = \det \mathbf{F}_e$, p is a Lagrange multiplier that ensures the incompressibility of the sample, a physical property assumed in living matter. If the cylinder contains several layers with different shear modulus μ and different active strains, the integral over S covers each layer. To minimize the energy over each section for a given active force, we take advantage of the small value of ε and expand the inner variables a, p, and the potential V to obtain the associated strain-energy density. Since the Euler-Lagrange equations and the boundary conditions are satisfied at each order, we can obtain solutions for the elastic strains at zero order $\mathbf{a^{(0)}}$ and at first order $\mathbf{a^{(1)}}$. Finally, these solutions which will represent a combination of bending and torsional deformation, will last for the duration of a muscle contraction as the actomyosin continues its contractile activity. The evaluation of the elastic energy under actomyosin muscle activity of order ε^4 can be compared with the equivalent energy of an extensible elastic rod and any fundamental deformation will be identified (***Kirchhoff and Hensel*** (***1883***); ***Mielke*** (***1988***); ***Mora and Müller*** (***2002***, 2004); ***Moulton et al.*** (***2020a***)). The typical quantities of interest are the curvature achieved during a bending event or a torsion as well as the total elongation ζ. In the *C. elegans* embryonic system, these quantities result from the competition between the active strains due to muscles and the myosin motors and the elasticity of the body. Similar active matter can be found in biological systems, from animals to plants, as illustrated in Fig.4(A)-(C), they have a structure that generates internal stress/strain for the growth or daily activities. By combining anatomy and measurement techniques, we can transform the mechanics of the body under study into a soft sample subjected to localized internal active stresses or localized internal active strains and then deduce its overall deformation mechanisms, some examples are presented in Fig.4(D)-(F).

The early elongation induced by the actomyosin

Experimental measurements during the early elongation stage reveal the embryonic diameter and the active or passive stresses, estimated by the opening of fractures realized in the body by laser ablation (***Vuong-Brender et al.*** (***2017a***); ***Ben Amar et al.*** (***2018***)). These quantities vary with the elongation. While previous studies have extensively investigated this initial stage, we have chosen to revisit it in the context of our geometry, with the goal of achieving complete control over our structural modeling, which includes the geometry, shear modulus, and activity of the actomyosin prior to muscle contraction. At the beginning of the second stage, the embryo experiences a pre-strain due to the early elongation, which we describe in our model as $\mathbf{G}_0$. The geometry and mechanical information are depicted in Fig.5(A).

Here, we must first accurately determine $\mathbf{G}_0$ by analyzing the experimental data (***Vuong-Brender et al.*** (***2017a***); ***Ben Amar et al.*** (***2018***)). The cylinder can be divided into three distinct sections: the outer layer is the actin cortex, the thin ring where actin bundles concentrate and work, located within a radius range between $R_2{}'$ and R_3 (as shown in Fig.5(A)); the middle layer ($R_2 < R < R_2{}'$), which is the epidermis but without actin; and the inner part ($0 < R < R_2$), where the muscle is

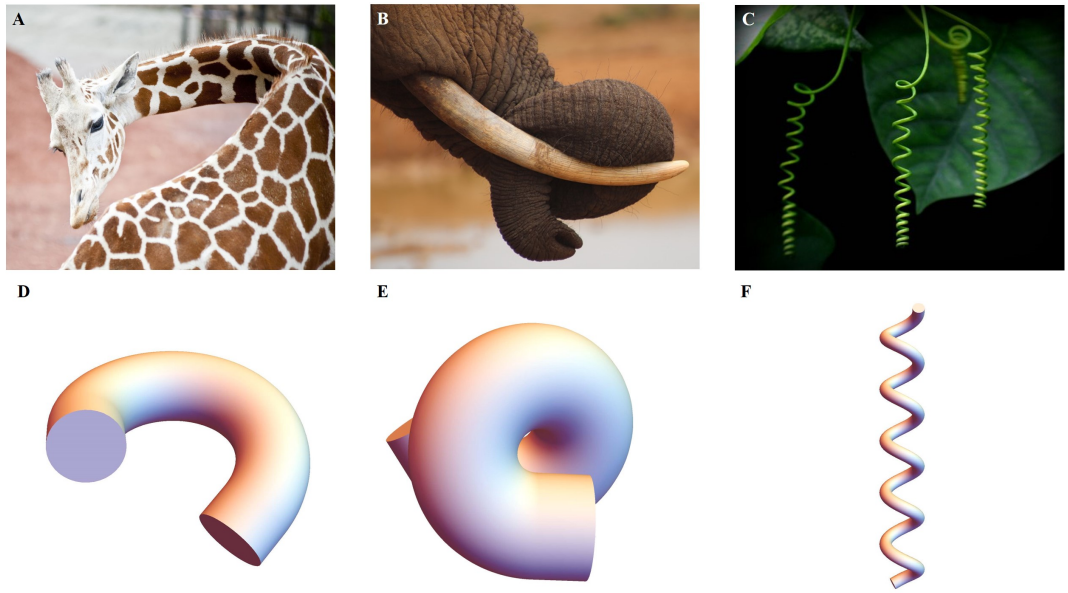

Figure 4. (A) Bending of a giraffe's neck. (B) Torsion of an elephant's trunk. (B) Twisting of a plant vine. (D) to (F) Deformation configuration under different activations obtained by our simulations for bending and torsion of large rods, twisting and torsion of thin rods.

located, along with some internal organs, tissues, and fluids. So, we treat the outer and middle layers as incompressible, but the inner part as a compressible material, except for the muscles. The initial deformation gradient: $\mathbf{F}_0$ =Diag$(r'(R), r(R)/R, \lambda)$, and $\mathbf{G}_0$ = Diag$(1, g_0, 1)$ with $0 < g_0 < 1$ in the actin layer, but with $g_0 = 1$ in the part without actin. $\mathbf{G}_0$ represents the circumferential strain exerted by actin during the early elongation and is a slowly varying function of time. By applying the principles of radius continuity, radial stress continuity, and incorporating the zero traction condition on the face of the cylinder, we can determine that $g_0 = 0.88$ when the elongation $\lambda = 1.8$, at the end of the early elongation. As illustrated in Fig.5(B), the results of our model and the experimental data are in good agreement, demonstrating the consistency of the geometric and elastic modeling together with the choice of a pre-strain represented by $\mathbf{G}_0$ which gives a good prediction of the early elongation. More details can be found in the appendix 3.

From the first stage elongation represented by the blue dots and the blue dashed line in Fig.5(C) we can extract the time evolution of the contractile pre-strain $g_0(t_i)$ derived from our elastic model. To explain $g_0(t)$ quantitatively , we propose a phenomenological dynamical approach for the population of active myosin motors. This equation takes into account the competition between the recruitment of new myosin proteins from the epidermal cytoskeleton, which is necessary to elongate the embryo, and the detachment of these myosins from the actin cables, which is damped by the compressive radial stress. It reads:

$$\frac{dX_g(t)}{dt} = \left(p_1 - p_2 X_g(t) e^{-p_3 X_g(t)}\right) \frac{t_v}{t_p} \tag{3}$$

where $X_g = 1 - g_0(t)$, p_1 is the ratio of the freely available myosin population to the attached ones divided by the time of recruitment (given in minutes), while p_2 is the inverse of the debonding time of the myosin motors from the cable: $p_2 = 6$ min^{-1}. The debonding time increases (or decreases) when the actin cable is under radial compressive (or tensile) stress, see Appendix 3, Eq.(35). τ_v is the viscoelastic time estimated from laser ablation fracture operated in the epidermis (***Vuong-Brender et al.*** (***2017b***)): $t_v = 6s$ and τ_p is the time required to activate the myosin motors $t_p = 1200s$ (***Howard and Clark*** (***2002***)). This equation is similar to the model derived by Serra *et al* (***Serra et al.*** (***2021***)) for the viscous stress that occurs during gastrulation.

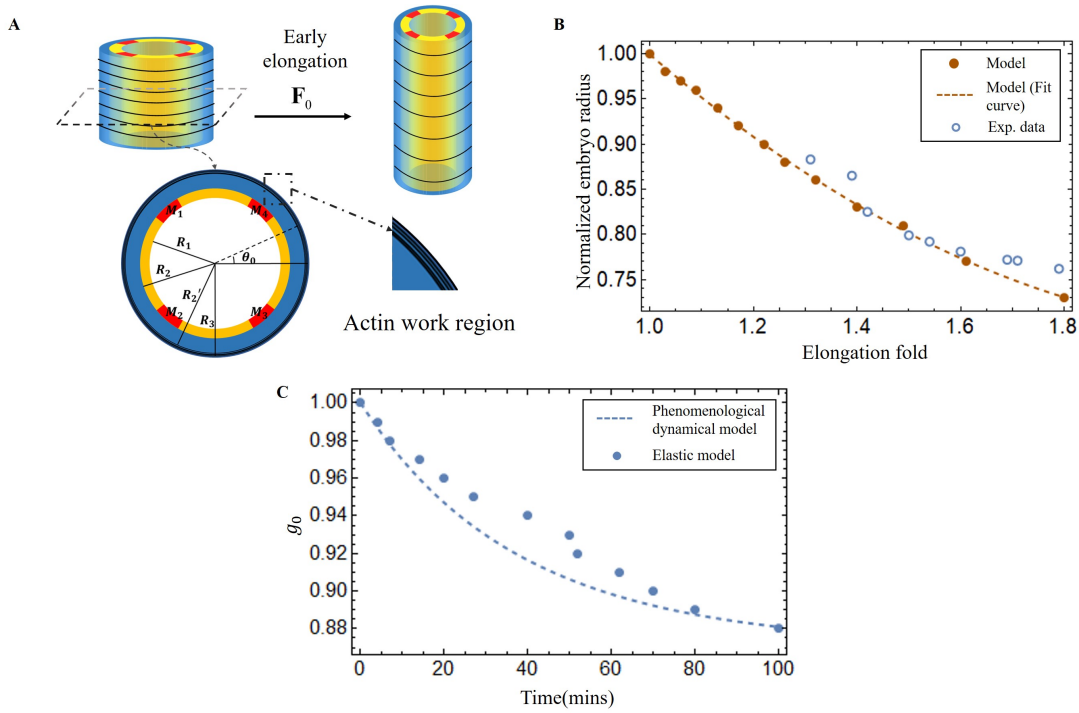

Figure 5. (A) Schematic of early elongation and the cross section of *C. elegans*. In the cross-section, the black circular part is the actin region ($R_2' < R < R_3$, with shear modulus μ_a), the blue part is the epidermis layer ($R_2 < R < R_2'$ with shear modulus μ_e). The central or inner part ($0 < R < R_2$ in white has shear modulus μ_i, except for the four muscles, the shear modulus of the four muscles μ_m is much larger than the inner part. (B) Predictions of normalized embryo radius evolution during early elongation by the pre-strain model compared to experimental data from (***Vuong-Brender et al.*** (***2017a***)). For the model, see Eq.(20) in Appendix 2. (C) Blue dots: extraction of the parameter $g_0(t)$ from Eq.(30) and Eq.(32) in Appendix 2. Blue dash line, see Eq.(3).

Note that only p_1 and p_3 need be obtained by comparing $g_0(t)$ deduced from Eq.(3) with the values derived from our elastic model. The result of Eq.(3) with $p_1 = 0.6$ and $p_3 = 0.75$ are shown in Fig.5(C) with a rather good agreement.

Shape of the embryo under muscles and actomyosin contraction

The experimental regulation of muscle contraction in *C. elegans* (***Yang*** (***2017***)) suggests a cyclic process in which two muscles on one side of the embryo contract quite at the same time and then stop, while on the opposite side the two muscles begin to contract, but with a delay. Let us first consider that only the muscles are active (see the schematic Fig.6(A) for the structure, then (B) and (C) for the bending). In this case, due to the geometry, bending to the left occurs when the left muscles are activated and then to the right for the symmetrical right muscles.

To be more quantitative, we assume that the left side muscles are activated during a short period with an active constant strain value g_m in the region M_1 and M_2, as shown in Fig.6(A)-(B); if the muscles are perfectly vertical, $\alpha_m = \beta_m = 0$ in the initial configuration. In fact, the two muscles on the same side are not always completely in phase, and one may have a small delay. For simplicity, we assume that they contract simultaneously. During the entire initial period when the muscles are not activated, the actin fibers are distributed in a horizontal loop on the outer surface of the epidermis, but as soon as the muscle starts to contract, the actomyosin network will be reoriented (***Lardennois et al.*** (***2019***)). The fibers are then distributed in an oblique pattern, which eventually causes the twisting of the embryo, see the schematic diagram in Fig.6(D)-(F). When this region is activated with a constant strain value, g_a, the angle of the actin fibers will change according to the amplitude of the bending caused by the muscle contraction. In this situation, the angle of the actin

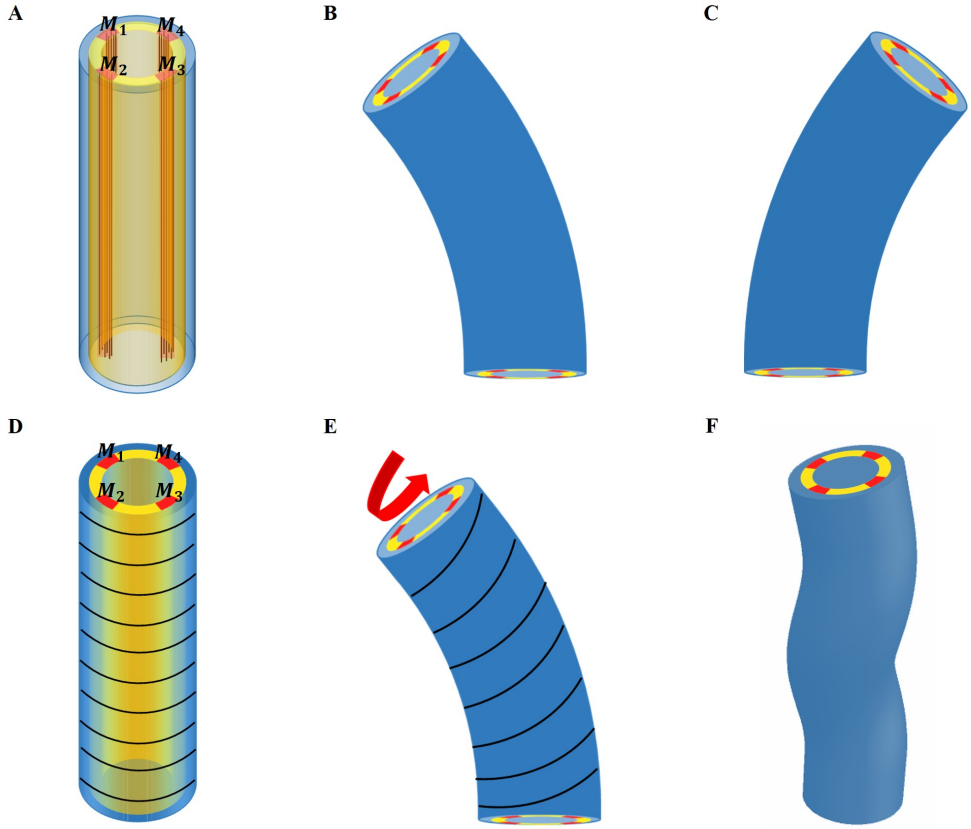

Figure 6. (A) Schematic diagram of *C. elegans* muscle fibers and its cross section, and it does not show the actin fibers. There are four muscle bands exist in the yellow layer. However, the yellow region is not an actual tissue layer and it is only used to define the position of the muscles. (B) Deformation diagram, left side muscles M_1 and M_2 are activated. (C) Deformation diagram, right side muscles M_3 and M_4 are activated. (D) Schematic diagram of *C. elegans* actin fibers and cross section. (E) Once the muscle is activated, the actin fiber orientation changes from the 'loop' to the 'slope', resulting in torque. (F) Schematic diagram of torsional and bending deformation.

fibers may change from $\alpha_a \in \left[0, \frac{\pi}{2}\right]$, but β_a is not changed and $\beta_a = 0$.

Throughout the entire process, the muscle and actomyosin activities are assumed to operate simultaneously. Our modeling allows us to evaluate the bending and torsion generated independently by muscles and actin bundles, culminating in a complete deformation under coupling. Furthermore, the angle of the actomyosin fibers varies during muscle contraction. We maintain a constant activation of the actomyosin network and gradually increase the muscle activation.

As a result, the structure will be bent, causing a change in the angle of the actin fibers, ultimately yielding a deformation map that is presented in Fig.7(A)-(C). As myosin activation increased, we observed a consistent torsional deformation (Fig.7(E)) that agrees with the patterns seen in the video (Fig.7(D)). However, significant torsional deformations are not always present. In fact, other sources can induce torsion as a default symmetry of the muscle axis. We will now discuss torsion due to muscle contraction and the angle of deviation from the axis. In Fig.7(F)-(G), we demonstrate that the curvature provided by the model increases with increasing muscle activation increases and that the torsion is not simply related to the activation amplitude, as it also depends on the value of the angle α_a, reaching a maximum at about $\pi/4$. Detailed calculations are given in Section Methods and Materials and Appendix 4.

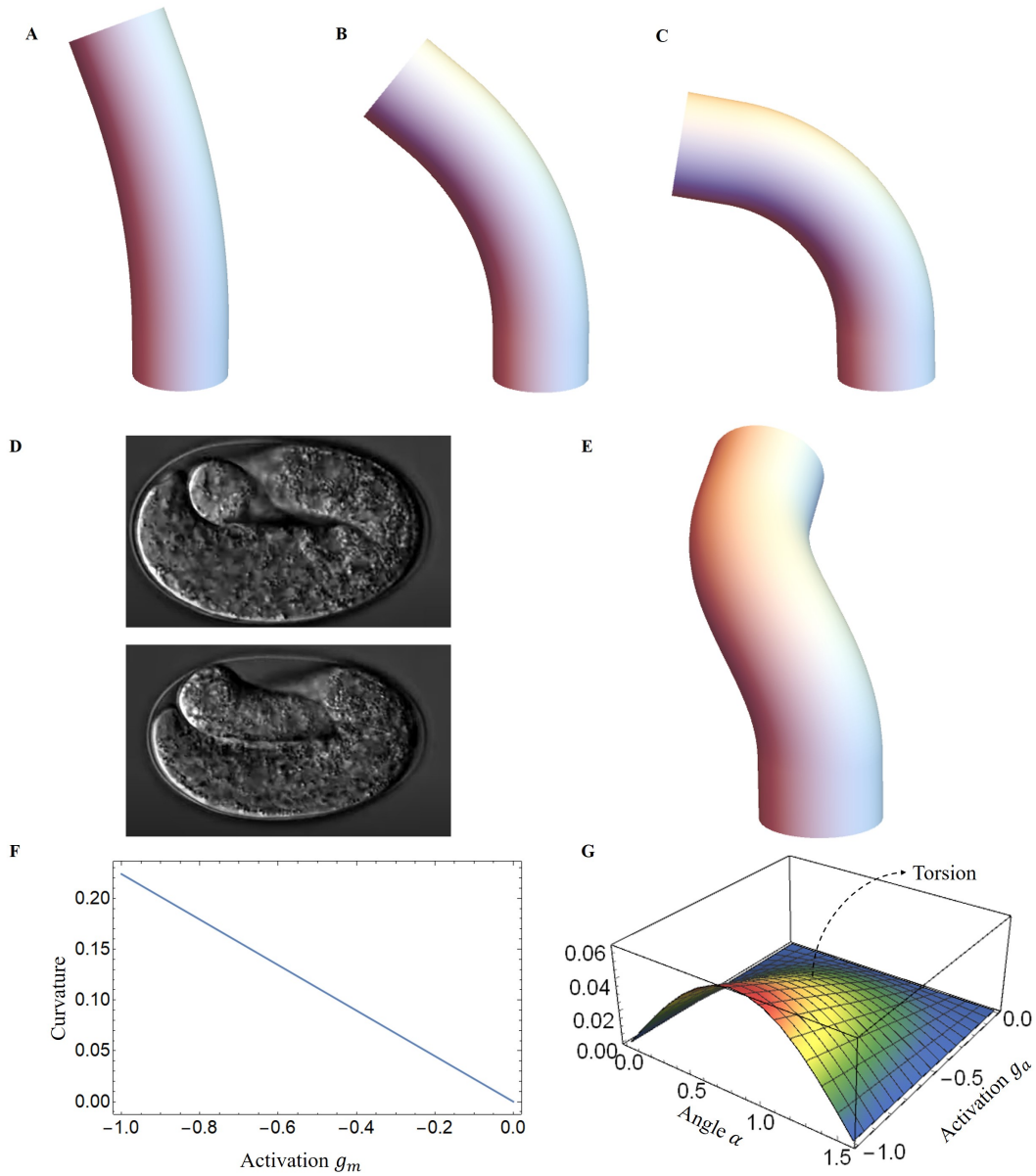

Figure 7. Deformed configurations for different activation for muscles, (A) $g_m = -0.02, \alpha_a = \pi/3, g_a = -0.01$. (B) $g_m = -0.05,\ \alpha_a = \pi/4,\ g_a = -0.01$. (C) $g_m = -0.08,\ \alpha_a = \pi/6,\ g_a = -0.01$. (D) The graphs were captured from the Hymanlab, and the website: https://www.youtube.com/watch?v=M2ApXHhYbaw. The movie was acquired at a temperature of 20^0C using DIC optics. (E) $g_m = -0.1,\ \alpha_a = \pi/4,\ g_a = -0.7$. (F) Curvature is plotted as a function of muscle activation. (G) Torsion is plotted as a function of the actin activation and angle of actin fibers.

Energy transformation and Elongation

During the late elongation process, the four internal muscle bands contract cyclically in pairs (***Yang*** (***2017***); ***Williams and Waterston*** (***1994***)). Each contraction of a pair increases the energy of the system under investigation, which is then rapidly released to the body. This energy exchange causes the torsional bending energy to be converted into elongation energy, leading to an increase in length during the relaxation phase, as shown in Fig.1 of the Appendix 5. With all the deformations obtained, Eq.(2) can be used to calculate the accumulated energy W_c produced by both the muscle and the actomyosin activities during a contraction. Subsequently, when the muscles on one side relax, the worm body returns to its original shape but with a tiny elongation corresponding to the

transferred elastic energy. In this new state, the actin network assumes a 'loop' configuration with a strain of εg_{a1} once relaxation is complete. If all the accumulated energy from the bending-torsion deformation is used to elongate the worm body, the accumulated energy W_c and the energy W_r after muscle relaxation are equivalent. The activation of actin fibers g_{a1} after muscle relaxation can be calculated and determined by our model.

Once the first phase is well characterized, we can quantify the total energy resulting from both muscle and actomyosin after each contraction. We then used our model to predict elongation in wild type *C. elegans*, unc-112(RNAi) mutant and spc-1(RNAi) pak-1(tm403) mutant and further compared the results with experimental observations. The wild-type length increases from about $90\ \mu m$ to $210\ \mu m$ during the muscle-activated phase (***Lardennois et al.*** (***2019***)), the phase lasts about 140 minutes, and the average time interval between two contractions is about 40 seconds (***Yang*** (***2017***)), so the number of contractions can be estimated to be about 210 times. Unfortunately, due to the difficulty of performing quantitative experiments on an embryo that is constantly moving in the egg shell between bending, torsion, and even rotations around its central axis, one can hypothesize this scenario: at each step i between the state $A_{i,0}$ to $A_{i,1}$ and then $A_{i,2}$, the whole mechanical muscle-myosin energy is transferred to the elongated step $A_{i,2}$, resulting a small $\delta\zeta_i$.

Considering the experimental results shown in Fig.8(B), we determine the optimal values for the activation parameters: $g_m = -0.15$ and $g_a = -0.01$ assuming that all the energy accumulated during the muscle activation is transferred to the elongation process ($W_r = W_c$). The elementary elongation $\delta\zeta_i$ is gradually increased over time, which is shown as the black line in Fig.8(A). At the beginning, $\delta\zeta_i$ is about $0.5\mu m$, but at the end of this process, $\delta\zeta_i$ is about $1.5\mu m$, indicating that the worm will grow up to $290\mu m$. The result is significantly larger than our actual size $210\mu m$. As the elongation progresses, we assume that there is an energy transfer between bending-torsion-contraction and elongation but it may not be fully effective, meaning that a significant part of the energy is lost. From the experimental data, we estimate that the energy loss gradually increases, from full conversion at the beginning to only 40% of the accumulated energy used for elongation at the end of the process ($W_r = 0.4W_c$). For $\delta\zeta_i$ it induces a first increase and then a decrease, which is shown as the blue line in Fig.8(A) and is responsible for the slowdown around 200 mins. This possibility, which may be not the only possible one, leads to the estimated elongation being in good agreement with the experimental data (see the blue-dashed curve in Fig.8(B)). Indeed it is possible that the *C. elegans* elongation requires other transformations that cost energy. As the embryo gradually elongates, energy dissipation and the biomechanical energy required to reorganize the actin bundles may be two factors contributing to the increased energy loss underlying the hypothesis.

In addition, it has been reported in (***Norman and Moerman*** (***2002***)) that the knockdown of unc-112(RNAi), known the to affect muscle contractions, leads to the arrest of elongation of the embryos at the twofold stage, indicating that the muscles have no activation, $g_m = 0$ in our model, and no accumulated energy can be converted into elongation. Another mutation affecting the embryos consisting of mutant cells with pak-1(tm403), known to regulate the activity of myosin motors leads to a retraction of the embryo, so that the pre-stretch caused by myosin is not maintained and decreases. The results are fully consistent with a number of experimental observations and are shown in Fig.8(B).

Embryo rotations and dissipation

The main manifestation of the muscle activity, independent of the elongation, is probably the constant rotation of the embryo despite its confinement in the egg. This can be explained by a small angular deviation of the muscle sarcomeres from the central axis due to their attachment to the inner boundary of the cell epidermis, the so-called "dense bodies" (***Moerman and Williams*** (***2006***)). Since they cross the horizontal plane at about $\pm 45°$ and the deviation β_m from the anterior-posterior axis is estimated to be about $6°$ each active muscle on the left (or on the right) contributes to the torque via a geometric factor of about $a_g = \sin(6\pi/180)\cos(\pi/4)$. Then a simple estimate of muscle activity in terms of torque is $\Lambda_m \sim \mu_m \pi R^3 s_m p_m a_g(\varepsilon g_m)$ where s_m is the area of the left or right mus-

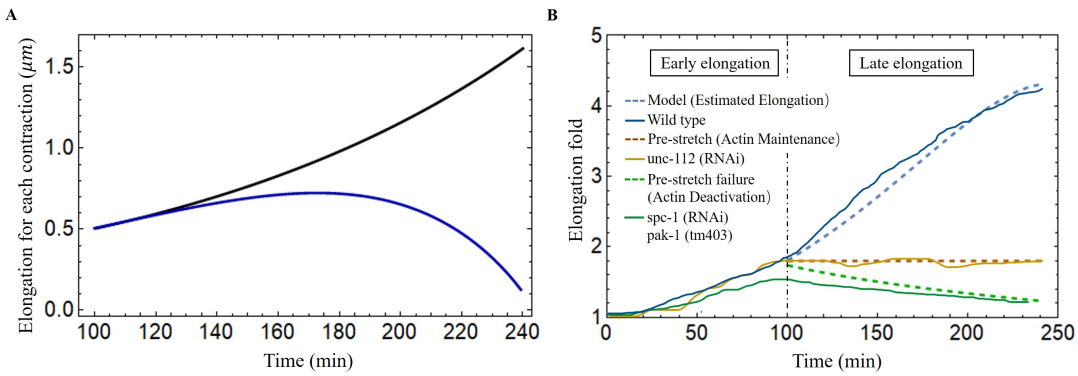

Figure 8. (A) The elongation for each contraction varies with time. Black line: all energy converted to the elongation, blue line: partial energy converted to the elongation. The activation: $g_m = -0.15$, $g_a = -0.01$. (B) The model predicted results agree well with the experimental data of wild-type and different mutant *C. elegans* embryos (***Lardennois et al.*** (***2019***)). Activation of the wild-type model (blue dashed line): $g_m = -0.15$, $g_a = -0.01$. The activation of unc-112(RNAi) (brown dashed line): $g_m = 0$, $g_a = 0$. In the case of pre-stretch failure (green dashed line), λ decreases from 1.8.

cle pair compared to the section of the cylinder: $s_m = 0.025$ and p_m is the distance of the muscles from the central axis of the embryo: $p_m = 0.75$ while $g_m = 0.15$ according to the elongation analysis . So the muscles on one side contribute to a torque Λ_m along the symmetry axis, given by $\Lambda_m = 4.657\mu_m \pi R^3 \cdot 10^{-5}$.

Let us now consider the dissipative torque, assuming that the rotational dynamics are stopped by friction after a bending event. Two cases can be considered: either the dissipation comes from the viscous flow or from the rubbing of the embryo when it folds. The fluid dissipation results from the rotations in the interstitial fluid inside and along the eggshell as the anterior-posterior axis remains parallel to the eggshell (***Bhatnagar et al.*** (***2023***)) The interstitial fluid, of viscosity η contains a significant amount of sugars and other molecules necessary for embryo survival and that is more viscous than water (***Labouesse*** (***2023***)). However, values for sucrose or sorbitol at the concentration of 1 mole/liter indicate a viscosity on the order of a few times the viscosity of water, which is 1 mPas. For example at 0.9 mole/liter and temperature of $20°$, an aqueous solution of sorbitol has a viscosity of 1.6 mPas, which can be extrapolated to $\eta = 1.9$ mPas at 1.2 mole/liter (***Jiang et al.*** (***2013***)). The estimate given by an embryo located in the middle of the egg shell, gives a weaker viscous torque once evaluated by $\Lambda_v = 4\pi\eta\Omega_e L R^2 \left(R_{egg}^2/(R_{egg}^2 - R^2) \right)$ according to a classical result reported by Landau *et al.* (***Landau and Lifshitz*** (***1971***, 2013)).

It should be noted that this estimation assumes that the two cylinders: the egg shell and the embryo have the same axis of symmetry and concerns the beginning of the muscle activity where the radius is about $8.2\,\mu m$, the length is $90\,\mu m$, the radius of the shell is about $R_{egg} = 15\mu m$ and the length $L_{egg} = 54\mu m$, see Fig.7(D). The angular velocity Ω_e is more difficult to evaluate but it is about $90°$ per two seconds deduced from videos. As the embryo approaches the eggshell, the friction increases, and two eccentric cylinders of different radii must be considered with the two symmetry axes separated by a distance d. The hydrodynamic study in this case is far from being trivial, and seems to have been first initiated by Zhukoski (***Zhukoski*** (***1887***)), who proposed the use of bipolar coordinates for the mathematical treatment. Many subsequent papers were published after, using barious simplified assumptions, and the study was completely revisited by Ballal and Rivlin (***Ballal and Rivlin*** (***1976***)). Here we focus on the limit of a small gap δ between the rotating body shape and the egg and by considering an asymptotic analysis at small δ of the general result derived in (***Ballal and Rivlin*** (***1976***)). Thus, the viscous torque reads $\tilde{\Lambda}_v = 2\sqrt{2}\pi\eta\Omega_e L_c R_{egg}^2 \sqrt{R_{egg}/\delta}\sqrt{(R_{egg} - d)/d}$, where L_c is the zone of contact with the egg and $d = R_{egg} - \delta - R$. This approach is an approximation since the embryo is more toroidal than cylindrical (***Yang Xinyi et al.*** (***2023***)), but the evaluation of

the dissipation is satisfactory for $\delta = 0.5\mu m, \Omega_e \sim \pi/4\, s^{-1}$ and $\mu = 10^5 Pa$. Going back back to the first model of dissipation with the same data, the ratio between the dissipative viscous torque and the active one gives: $\Lambda_v/\Lambda_m = 0.02$, which is obviously unsatisfactory. Finally, the dissipative energy $\mathcal{E}_{diss}$ during one bending event leading to an angle of $\pi/2$ is $\mathcal{E}_{diss} = 1/2\Lambda_m \times (\pi/2)^2$ which represents 4% of the muscle elastic energy during the bending so at the beginning of the muscle activity (Appendix 5, Eq.(45)), the dissipation is present but is negligible. At the very end of the process, this ratio becomes 60% but as already mentioned, our estimate for the dissipation becomes very approximate, increases a lot due to the embryo confinement, and does not include the numerous biochemical steps necessary to reorganize the active network: actomyosin and muscles.

Discussion

Since the discovery of the pre-embryonic muscle activity in the *C. elegans* embryo, it has become critical to explain the role of mechanical forces generated by muscle contraction on the behavioral and functional aspects of the epidermis. We provide a mechanical model in which the *C. elegans* is simplified as a cylinder, and the muscle bands and actin that drive its elongation are modeled as active structures in a realistic position. We determine the fiber orientation from experimental observations and then calculate the deformation by tensorial analysis using the strains generated by the active components. Although a special focus is given to late elongation, its quantitative treatment cannot avoid the influence of the first stage of elongation due to the actomyosin network, which is responsible for a pre-strain of the embryo. In a finite elasticity formalism, the deformations induced by the muscles in a second step are coupled to the level of strains of the initial elongation period. For this, we must revisit the theory of the actomyosin contraction and previous results (***Ciarletta et al.*** (***2009***); ***Vuong-Brender et al.*** (***2017a***); ***Ben Amar et al.*** (***2018***)) to unify the complete treatment. In particular, a model for the recruitment of active myosin motors under forcing is presented that recovers the experimental results of the first elongation phase

The elongation process of *C. elegans* during the late period is much more complex than the early elongation stage which is caused by actin contraction alone. During late elongation, the worm is deformed by the combined action of muscle and actomyosin, resulting in an energy-accumulating process. Bending deformation is a phenomenon resulting from unilateral muscle contraction, and during the late elongation, significant torsional deformation is observed, indicating that the bending process induces a reorientation of the actin fibers. It should be noted that the embryo always rotates in parallel to the muscle activity, which makes any experimental measurements difficult. However, our model can predict that if the muscles are not perfectly vertical,a torque is generated that causes rotation and eventually torsion. The accumulated energy is then partially converted into energy for the ongoing action of actin, allowing the embryo to elongate when the muscle relaxes. Both sides of the *C. elegans* muscles contract in a sequential cycle, repeating the energy conversion process, and eventually completing the elongation process. However, the energy exchange between bending and elongation is limited, among other factors, by the viscous dissipation induced by rotation, which is also evaluated in this study. The necessary reorganization of the active networks (actomyosin and muscles) due to this enormous shape change of the embryo is not investigated here in detail. Parallel to the elongation, the cuticle is built around the body (***Page and Johnstone*** (***2007***)). This very thin and stiff membrane provides protection and locomotion after hatching. Obviously, these processes will interfere with muscle activity. These two aspects, which intervene in the final stage of the worm's confinement, play a very important role at the interface between genetics, biochemistry, and mechanics.

Finally, the framework presented here not only provides a theoretical explanation for embryonic elongation in *C. elegans*, but can also be used to model other biological behaviors, such as plant tropism (***Moulton et al.*** (***2020b***)) and elephant trunk elongation (***Schulz et al.*** (***2022b***,a)) and bending. Our ideas could potentially be used in the emerging field of soft robotics, such as octopus leg inspired robots (***Kang et al.*** (***2012***); ***Nakajima et al.*** (***2013***); ***Calisti et al.*** (***2015***)), which are soft and their deformation is induced by muscle activation. We can reliably predict the deformation

by knowing the position of activation and the magnitude of fthe orces in the model. In addition, residual stresses can be incorporated into our model to achieve design goals.

Methods and Materials

The model has been presented in a series of articles by A. Goriely and collaborators (***Goriely and Tabor*** (***2013***); ***Moulton et al.*** (***2013***, 2020b); ***Kaczmarski et al.*** (***2022***); ***Goriely et al.*** (***2022***)). As one can imagine, this is far from trivial, and most of the literature on the subject concerns either full cylinders or cylindrical shells in torsion around the axis of symmetry, the case of bending is far from trivial. However, the geometry of the muscles in *C. elegans* automatically leads to a bending process that cannot be discarded. We take advantage of these previous works and apply the methodology to our model.

The deformation gradient

The finite strain $\mathbf{G}_0$ maps the initial stress-free state $\mathcal{B}_0$ to a state $\mathcal{B}_1$, which describes the early elongation. We then impose an incremental strain filed $\mathbf{G}_1$ that maps the state $\mathcal{B}_1$ to the state $\mathcal{B}_2$, which represents late elongation. So, the deformation gradient can be expressed as: $\mathbf{F} = \mathbf{F}_e\mathbf{G}_1\mathbf{G}_0$ (***Goriely and Ben Amar*** (***2007***)). The deformation gradient $\mathbf{F} = F_{ij}\mathbf{d}_i \otimes \mathbf{e}_j,\ \ i \in \{1,2,3\}$ and j labels the reference coordinates $\{R, \Theta, Z\}$ finally reads:

$$\mathbf{F} = \begin{bmatrix} a_{1R} & \frac{1}{R}a_{1\Theta} & \lambda\varepsilon\left(1+\varepsilon\xi\right)\left(u_2a_3 - u_3a_1\sin a_2\right) \\ a_1a_{2R} & \frac{a_1}{R}a_{2\Theta} & \lambda\varepsilon\left(1+\varepsilon\xi\right)\left(u_3a_1\cos a_2 - u_1a_3\right) \\ a_{3R} & \frac{1}{R}a_{3\Theta} & \lambda\left(1+\varepsilon\xi\right)\left(1+\varepsilon\left(u_1a_1\sin a_2 - u_2a_1\cos a_2\right)\right) \end{bmatrix}, \tag{4}$$

where λ is the axial extension due to the pre-strained.

We define $\mathbf{G}_0 = Diag\left(1, 1+\varepsilon c, 1\right)$, since $g_0 = 0.88$ can be determined by the early elongation, we write it in the form of $1+\varepsilon c$ to simplify the calculation, $c \approx -0.6$ ($\varepsilon \approx 0.2$).

Consider fibers oriented along the unit vector $\mathbf{m} = (\sin\alpha\sin\beta, \sin\alpha\cos\beta, \cos\alpha)$ for the incremental strain $\mathbf{G_1}$, where α and β characterize the angles with $\mathbf{e_z}$ and $\mathbf{e}_\theta$ and can be found in Fig.3(A). The active filamentary tensor in cylindrical coordinates is then $\mathbf{G} = \mathbf{G}_0\left(\mathbf{I} + \varepsilon g\ \mathbf{m}\otimes\mathbf{m}\right)$, see (***Holzapfel*** (***2000***)) which reads:

$$\mathbf{G} = \mathbf{G_0} + \varepsilon g\mathbf{G_0}\begin{bmatrix} \sin^2\alpha\sin^2\beta & \sin^2\alpha\sin\beta\cos\beta & \sin\alpha\cos\alpha\sin\beta \\ \sin^2\alpha\sin\beta\cos\beta & \sin^2\alpha\cos^2\beta & \sin\alpha\cos\alpha\cos\beta \\ \sin\alpha\cos\alpha\sin\beta & \sin\alpha\cos\alpha\cos\beta & \cos^2\alpha \end{bmatrix}. \tag{5}$$

The energy function

The associated strain-energy density can be obtained by expanding the inner variables a_i (see Eq.(1)), p_i and the potential V (see Eq.(2)) as:

$$\mathbf{a} = \mathbf{a}^{(0)} + \varepsilon\mathbf{a}^{(1)} + \varepsilon^2\mathbf{a}^{(2)} + \mathcal{O}\left(\varepsilon^3\right), \tag{6}$$

$$p = p^{(0)} + \varepsilon p^{(1)} + \varepsilon^2 p^{(2)} + O\left(\varepsilon^3\right), \tag{7}$$

$$V(\mathbf{F}_e, \mathbf{G}) = V_0 + \varepsilon V_1 + \varepsilon^2 V_2 + O\left(\varepsilon^3\right). \tag{8}$$

For each cross section, the associated Euler-Lagrange equations take the following form:

$$\frac{\partial}{\partial R}\frac{\partial V_iR}{\partial a^{(k)}_{jR}} + \frac{1}{R}\frac{\partial V_iR}{\partial a^{(k)}_{jR}} + \frac{\partial}{\partial\Theta}\frac{\partial V_iR}{\partial a^{(k)}_{j\Theta}} - \frac{\partial V_iR}{\partial a^{(k)}_{j}} = 0, \tag{9}$$

where $j = 1,2,3, k = 0,1$, in association with boundary conditions at each order $k = 0,1$ on the outer radius R_i:

$$\left.\frac{\partial V_iR}{\partial a^{(k)}_{jR}}\right|_{R=R_i} = 0, j = 1,2,3. \tag{10}$$

We solve these equations order by order, taking incompressibility into account. At the lowest order, the incompressibility imposes the deformation: $\mathbf{a}^{(0)} = (r(R), \Theta, 0)$ and the Euler-Lagrange equation gives the Lagrange parameter $p^{(0)} = P_0(R)$ which finally read:

$$r' = \frac{R}{\lambda r},\ P_0{}' = 0, \tag{11}$$

and the boundary condition $\sigma_{rr}(R=1) = 0$ gives the value of $P_0 = 1/\lambda$. At $\mathcal{O}(\varepsilon)$, the Euler-Lagrange equations are again automatically satisfied, and at $\mathcal{O}\left(\varepsilon^2\right)$, the crucial question is to get the correct expression for $a_i^{(1)}$ and $p^{(1)}$. Based on the previous subsection, the following form is intuited:

$$\begin{aligned}
a_1^{(1)} &= -\frac{1}{2} r(R)\,\xi + q_1 r(R)^2 \left(u_1 \sin\Theta - u_2 \cos\Theta\right) + h_1(R) \\
a_2^{(1)} &= q_2 r(R) \left(u_1 \cos\Theta + u_2 \sin\Theta\right) + h_2(R) \\
a_3^{(1)} &= \lambda \xi \\
p^{(1)} &= h_3(R)
\end{aligned} \tag{12}$$

As before, the Euler-Lagrange equations and the incompressibility condition give the two constants $q_1 = \frac{1}{8}\left(-2+\lambda^3\right)$, $q_2 = \frac{1}{8}\left(2+3\lambda^3\right)$ and h_1, h_2, h_3 are a function of R. With the solutions for active strain $\mathbf{a}^{(0)}$ and $\mathbf{a}^{(1)}$, full expressions of them are given in the Appendix 4. The second order energy takes the form:

$$\mathcal{E} = \varepsilon^4 \int_0^L \mathrm{d}Z \int_S V_2\left(\mathbf{a}^{(0)}, \mathbf{a}^{(1)}; \mathrm{u}_1, \mathrm{u}_2, \mathrm{u}_3, \xi\right) R\mathrm{d}R\ \mathrm{d}\Theta + \mathcal{O}\left(\varepsilon^5\right), \tag{13}$$

and we can transform it into this form:

$$V_2 R = A_1\xi + A_2\xi^2 + B_1 u_1 + B_2 {u_1}^2 + C_1 u_2 + C_2 {u_2}^2 + D_1 u_3 + D_2 {u_3}^2, \tag{14}$$

where A_i, B_i, C_i and D_i are functions of R and Θ.

The method for determining deformation

Comparing with the energy of an extensible elastic rod (***Moulton et al.*** (***2020a***); ***Kirchhoff and Hensel*** (***1883***); ***Mielke*** (***1988***); ***Mora and Müller*** (***2002***, 2004)), we recognize the classic extensional stiffness K_0, bending stiffness K_1 and K_2, torsional stiffness K_3 coefficients:

$$K_0 = \int_{S_K} A_2 d\,R d\Theta,\ K_1 = \int_{S_K} B_2 d\,R d\Theta,\ K_2 = \int_{S_K} C_2 d\,R d\Theta,\ K_3 = \int_{S_K} D_2 d\,R d\Theta, \tag{15}$$

where A_2, B_2, C_2 and D_2 are related to the shear modulus μ, so for a uniform material with no variations of shear modulus, S_K represents the cross section of the cylinder. But if not, we need to divide different regions to perform the integration.

We now focus on the intrinsic extension and curvature of the cylindrical object induced by the active strains, which requires the competition of the active forces with the stiffness of the cylindrical beam according to the relationships,

$$\hat{\zeta} = 1 - H_0/K_0,\ \hat{u}_1 = -H_1/K_1, \hat{u}_2 = H_2/K_2,\ \hat{u}_3 = -H_3/K_3, \tag{16}$$

where H_i calculated by:

$$H_0 = \frac{1}{2}\int_{S_H} A_1 d\,R d\Theta,\ H_1 = \frac{1}{2}\int_{S_H} B_1 d\,R d\Theta,\ H_2 = \frac{1}{2}\int_{S_H} C_1 d\,R d\Theta,\ H_3 = \frac{1}{2}\int_{S_H} D_1 d\,R d\Theta. \tag{17}$$

where A_1, B_1, C_1 and D_1 are related to the shear modulus μ,the fiber angles α and β, and the activation g. So, the integration region S_H is divided into the different parts of the embryo which all contribute to the deformation.

To calculate the intrinsic Frenet curvature and torsion, we use the following equation:

$$\hat{\kappa} = \sqrt{\hat{u}_1^2 + \hat{u}_2^2} \quad \text{and} \quad \hat{\tau} = \frac{\hat{u}_3}{\hat{\zeta}}. \tag{18}$$

Finally, in the case of the activated left side muscles, we can calculate the intrinsic extension and curvatures using Eq.(16), $\hat{u}_{1m} = 0$ and $\hat{u}_{3m} = 0$, so Frenet's intrinsic curvature and torsion Eq.(18), $\hat{\kappa}_m = \hat{u}_{2m}$ and $\hat{\tau}_m = 0$. For the activated actin case, we can calculate the intrinsic extension and curvatures by Eq.(16), $\hat{u}_{1a} = 0$ and $\hat{u}_{2a} = 0$, and the Frenet's intrinsic curvature and torsion Eq.(18), $\hat{\kappa}_a = 0$ and $\hat{\tau}_a = \frac{\hat{u}_{3a}}{\hat{\xi}_a}$. These quantities have been used to calculate the deformation images, as shown previously in Fig.7.

After obtaining all solutions, we can use these quantities to calculate the accumulated energy W_c in the system after one contraction by Eq.(2). By defining the activation (g_m and g_a) and the energy conversion efficiency , we can obtain the activation (g_{a1}) of the actin bundles after a single contraction and further calculate the elongation.

All calculation results and parameters are presented in the Appendix.

Acknowledgments

It is a pleasure to acknowledge fruitful discussions with Michel Labouesse and Kelly Molnar on experimental observations concerning the embryonic *C.elegans* elongation. We also thank Alain Goriely for his help with the technical aspects of nonlinear elasticity. Both authors acknowledge the support of the contract EpiMorph (ANR-2018-CE13-0008). Anna Dai acknowledges the support of the CSC (China Scholarship Council), file No. 201906250173.

References

Ballal B, Rivlin R. Flow of a Newtonian fluid between eccentric rotating cylinders: inertial effects. Archive for Rational Mechanics and Analysis. 1976; 62:237–294.

Ben Amar M, Bordner A. Mimicking cortex convolutions through the wrinkling of growing soft bilayers. Journal of Elasticity. 2017; 129(1):213–238.

Ben Amar M, Jia F. Anisotropic growth shapes intestinal tissues during embryogenesis. Proceedings of the National Academy of Sciences. 2013; 110(26):10525–10530.

Ben Amar M, Qiuyang-Qu P, Vuong-Brender TTK, Labouesse M. Assessing the contribution of active and passive stresses in C. elegans elongation. Physical Review Letters. 2018; 121(26):268102.

Bertet C, Sulak L, Lecuit T. Myosin-dependent junction remodelling controls planar cell intercalation and axis elongation. Nature. 2004; 429(6992):667–671.

Bhatnagar A, Nestler M, Gross P, Kramar M, Leaver M, Voigt A, Grill SW. Axis convergence in C. elegans embryos. bioRxiv. 2023; p. 2023–03.

Blankenship JT, Backovic ST, Sanny JS, Weitz O, Zallen JA. Multicellular rosette formation links planar cell polarity to tissue morphogenesis. Developmental cell. 2006; 11(4):459–470.

Bouchard A, Hofland GW, Witkamp GJ. Properties of sugar, polyol, and polysaccharide water- ethanol solutions. Journal of Chemical & Engineering Data. 2007; 52(5):1838–1842.

Calisti M, Corucci F, Arienti A, Laschi C. Dynamics of underwater legged locomotion: modeling and experiments on an octopus-inspired robot. Bioinspiration & biomimetics. 2015; 10(4):046012.

Chadwick R. Slow viscous flow inside a torus—the resistance of small tortuous blood vessels. Quarterly of applied mathematics. 1985; 43(3):317–323.

Ciarletta P, Ben Amar M, Labouesse M. Continuum model of epithelial morphogenesis during Caenorhabditis elegans embryonic elongation. Philosophical Transactions of the Royal Society A: Mathematical, Physical and Engineering Sciences. 2009; 367(1902):3379–3400.

Ciarletta P, Ben Amar M. Papillary networks in the dermal–epidermal junction of skin: a biomechanical model. Mechanics Research Communications. 2012; 42:68–76.

Coulombre AJ, Coulombre JL. Intestinal development: I. Morphogenesis of the villi and musculature. Journal of Embryology and Experimental Morphology. 1958; 6(3):403–411.

Cowan CR, Hyman AA. Acto-myosin reorganization and PAR polarity in C. elegans. Development. 2007; 134(6):1035–1043.

De Vita R, Grange R, Nardinocchi P, Teresi L. Mathematical model for isometric and isotonic muscle contractions. Journal of Theoretical Biology. 2017; 425:1–10.

Denham JE, Ranner T, Cohen N. Signatures of proprioceptive control in Caenorhabditis elegans locomotion. Philosophical Transactions of the Royal Society B: Biological Sciences. 2018; 373(1758):20180208.

Gally C, Wissler F, Zahreddine H, Quintin S, Landmann F, Labouesse M. Myosin II regulation during C. elegans embryonic elongation: LET-502/ROCK, MRCK-1 and PAK-1, three kinases with different roles. Development. 2009; 136(18):3109–3119.

Goriely A. The mathematics and mechanics of biological growth, vol. 45. Springer; 2017.

Goriely A, Ben Amar M. On the definition and modeling of incremental, cumulative, and continuous growth laws in morphoelasticity. Biomechanics and modeling in mechanobiology. 2007; 6(5):289–296.

Goriely A, Geers MG, Holzapfel GA, Jayamohan J, Jérusalem A, Sivaloganathan S, Squier W, van Dommelen JA, Waters S, Kuhl E. Mechanics of the brain: perspectives, challenges, and opportunities. Biomechanics and modeling in mechanobiology. 2015; 14(5):931–965.

Goriely A, Moulton DE, Angela Mihai L. A rod theory for liquid crystalline elastomers. Journal of Elasticity. 2022; p. 1–24.

Goriely A, Tabor M. Rotation, inversion and perversion in anisotropic elastic cylindrical tubes and membranes. Proceedings of the Royal Society A: Mathematical, Physical and Engineering Sciences. 2013; 469(2153):20130011.

Hannezo E, Prost J, Joanny JF. Instabilities of monolayered epithelia: shape and structure of villi and crypts. Physical Review Letters. 2011; 107(7):078104.

Hidayanto E, Tanabe T, Kawai J. Measurement of viscosity and sucrose concentration in aqueous solution using portable Brix meter. Berkala Fisika. 2010; 13(2):23–28.

Holzapfel GA. Nonlinear solid mechanics: a continuum approach for engineering science. Wiley; 2000.

Howard J, Clark R. Mechanics of motor proteins and the cytoskeleton. Appl Mech Rev. 2002; 55(2):B39–B39.

Jiang X, Zhu C, Ma Y. Density and viscosity of sorbitol/maltitol in L-ascorbic acid aqueous solutions at T=(293.15 to 323.15) K. Journal of Molecular Liquids. 2013; 188:67–73.

Kaczmarski B, Moulton DE, Kuhl E, Goriely A. Active filaments I: Curvature and torsion generation. Journal of the Mechanics and Physics of Solids. 2022; 164:104918.

Kang R, Branson DT, Guglielmino E, Caldwell DG. Dynamic modeling and control of an octopus inspired multiple continuum arm robot. Computers & Mathematics with Applications. 2012; 64(5):1004–1016.

Kirchhoff G, Hensel K. Vorlesungen über mathematische Physik, vol. 1. Druck und Verlag von BG Teubner; 1883.

Kücken M, Newell AC. Fingerprint formation. Journal of theoretical biology. 2005; 235(1):71–83.

Labouesse M. Viscosity of the intersticial fluid. The fluid contained in the embryo egg is a highly viscous solution full of diverse sugars and other molecules necessary for metabolism The proof is given by the necessity to put the embryo in a solution when the hatching is achieved on purpose The survival of the embryo lasts few hours The solution is a sorbitol aqueous solution containing approximately 1-12 mole/L. 2023; .

Landau L, Lifshitz E. Mécanique des fluides, editions Mir, vol. 6. Edition Mir; 1971.

Landau LD, Lifshitz EM. Fluid Mechanics: Landau and Lifshitz: Course of Theoretical Physics, Volume 6, vol. 6. Elsevier; 2013.

Lardennois A, Pásti G, Ferraro T, Llense F, Mahou P, Pontabry J, Rodriguez D, Kim S, Ono S, Beaurepaire E, et al. An actin-based viscoplastic lock ensures progressive body-axis elongation. Nature. 2019; 573(7773):266–270.

Lesanpezeshki L, Qadota H, Darabad MN, Kashyap K, Lacerda CM, Szewczyk NJ, Benian GM, Vanapalli SA. Investigating the correlation of muscle function tests and sarcomere organization in C. elegans. Skeletal muscle. 2021; 11(1):1–15.

Levayer R, Lecuit T. Biomechanical regulation of contractility: spatial control and dynamics. Trends in cell biology. 2012; 22(2):61–81.

Li B, Cao YP, Feng XQ, Gao H. Surface wrinkling of mucosa induced by volumetric growth: theory, simulation and experiment. Journal of the Mechanics and Physics of Solids. 2011; 59(4):758–774.

Lv C, Yang Y, Li B. Nano/micromotors in active matter. Micromachines. 2022; 13(2):307.

McKeown C, Praitis V, Austin J. sma-1 encodes a betaH-spectrin homolog required for Caenorhabditis elegans morphogenesis. Development. 1998; 125(11):2087–2098.

Mielke A. On Saint-Venant's problem for an elastic strip. Proceedings of the Royal Society of Edinburgh Section A: Mathematics. 1988; 110(1-2):161–181.

Moerman DG, Williams BD. Sarcomere assembly in *C. elegans* muscle. WormBook: The Online Review of C elegans Biology [Internet]. 2006; .

Mora MG, Müller S. Derivation of the nonlinear bending-torsion theory for inextensible rods by Gamma-convergence. preprint. 2002; .

Mora MG, Müller S. A nonlinear model for inextensible rods as a low energy Γ-limit of three-dimensional nonlinear elasticity. Annales de l'Institut Henri Poincaré C. 2004; 21(3):271–293.

Moulton D, Lessinnes T, Goriely A. Morphoelastic rods. Part I: A single growing elastic rod. Journal of the Mechanics and Physics of Solids. 2013; 61(2):398–427.

Moulton DE, Lessinnes T, Goriely A. Morphoelastic rods III: Differential growth and curvature generation in elastic filaments. Journal of the Mechanics and Physics of Solids. 2020; 142:104022.

Moulton DE, Oliveri H, Goriely A. Multiscale integration of environmental stimuli in plant tropism produces complex behaviors. Proceedings of the National Academy of Sciences. 2020; 117(51):32226–32237.

Nakajima K, Hauser H, Kang R, Guglielmino E, Caldwell DG, Pfeifer R. A soft body as a reservoir: case studies in a dynamic model of octopus-inspired soft robotic arm. Frontiers in computational neuroscience. 2013; 7:91.

Nardinocchi P, Teresi L. On the active response of soft living tissues. Journal of Elasticity. 2007; 88(1):27–39.

Norman KR, Moerman DG. α spectrin is essential for morphogenesis and body wall muscle formation in Caenorhabditis elegans. The Journal of cell biology. 2002; 157(4):665–677.

Olson MF, Sahai E. The actin cytoskeleton in cancer cell motility. Clinical & experimental metastasis. 2009; 26(4):273–287.

Page AP, Johnstone I. The cuticle. WormBook. 2007; .

Palumbo S, Benvenuti E, Fraldi M. Actomyosin contractility and buckling of microtubules in nucleation, growth and disassembling of focal adhesions. Biomechanics and Modeling in Mechanobiology. 2022; 21:1–14.

Priess JR, Hirsh DI. Caenorhabditis elegans morphogenesis: the role of the cytoskeleton in elongation of the embryo. Developmental biology. 1986; 117(1):156–173.

Rodriguez EK, Hoger A, McCulloch AD. Stress-dependent finite growth in soft elastic tissues. Journal of biomechanics. 1994; 27(4):455–467.

Saxena A, Denholm B, Bunt S, Bischoff M, VijayRaghavan K, Skaer H. Epidermal growth factor signalling controls myosin II planar polarity to orchestrate convergent extension movements during Drosophila tubulogenesis. PLoS biology. 2014; 12(12):e1002013.

Schulz A, Dimitriyev M, Singal K, Sordilla S, Sahin A, Boyle C, Higgins C, Matsumoto E, Hu D. Creating bio-inspired tissue mimics of African elephant trunks' wrinkled and folded skin. In: *APS March Meeting Abstracts*, vol. 2022; 2022. p. Z08–010.

Schulz AK, Boyle M, Boyle C, Sordilla S, Rincon C, Hooper S, Aubuchon C, Reidenberg JS, Higgins C, Hu DL. Skin wrinkles and folds enable asymmetric stretch in the elephant trunk. Proceedings of the National Academy of Sciences. 2022; 119(31):e2122563119.

Serra M, Nájera GS, Chuai M, Spandan V, Weijer CJ, Mahadevan L. A mechanochemical model recapitulates distinct vertebrate gastrulation modes. bioRxiv. 2021; p. 2021–10.

Shindo A, Wallingford JB. PCP and septins compartmentalize cortical actomyosin to direct collective cell movement. Science. 2014; 343(6171):649–652.

Shyer AE, Tallinen T, Nerurkar NL, Wei Z, Gil ES, Kaplan DL, Tabin CJ, Mahadevan L. Villification: how the gut gets its villi. Science. 2013; 342(6155):212–218.

Soesanto T, Williams MC. Volumetric interpretation of viscosity for concentrated and dilute sugar solutions. The journal of physical chemistry. 1981; 85(22):3338–3341.

Sulston JE, Schierenberg E, White JG, Thomson JN. The embryonic cell lineage of the nematode Caenorhabditis elegans. Developmental biology. 1983; 100(1):64–119.

Tallinen T, Chung JY, Rousseau F, Girard N, Lefèvre J, Mahadevan L. On the growth and form of cortical convolutions. Nature Physics. 2016; 12(6):588–593.

Tan T, De Vita R. A structural constitutive model for smooth muscle contraction in biological tissues. International Journal of Non-Linear Mechanics. 2015; 75:46–53.

Telis VRN, Telis-Romero J, Mazzotti H, Gabas AL. Viscosity of aqueous carbohydrate solutions at different temperatures and concentrations. International Journal of food properties. 2007; 10(1):185–195.

Toro R, Burnod Y. A morphogenetic model for the development of cortical convolutions. Cerebral cortex. 2005; 15(12):1900–1913.

Vicente-Manzanares M, Ma X, Adelstein RS, Horwitz AR. Non-muscle myosin II takes centre stage in cell adhesion and migration. Nature reviews Molecular cell biology. 2009; 10(11):778–790.

Vuong-Brender TTK, Ben Amar M, Pontabry J, Labouesse M. The interplay of stiffness and force anisotropies drives embryo elongation. Elife. 2017; 6:e23866.

Vuong-Brender TTK, Suman SK, Labouesse M. The apical ECM preserves embryonic integrity and distributes mechanical stress during morphogenesis. Development. 2017; 144(23):4336–4349.

Williams BD, Waterston RH. Genes critical for muscle development and function in Caenorhabditis elegans identified through lethal mutations. The Journal of cell biology. 1994; 124(4):475–490.

Yang X. Remodelage des jonctions sous stress mécanique. PhD thesis, Université de Strasbourg; 2017.

Yang Xinyi FT, Kelly Molnar NM, Loic Royer JP, Stephan Grill GM, Labouesse M. Planar asymmetry in epithelial junction elongation results from repeated muscle contraction events. Preprint Sorbonne University. 2023; .

Zhang H, Landmann F, Zahreddine H, Rodriguez D, Koch M, Labouesse M. A tension-induced mechanotransduction pathway promotes epithelial morphogenesis. Nature. 2011; 471(7336):99–103.

Zhukoski NE. Conference. Comm Math Soc Kharkov. 1887; 17:31–46.

Appendix 1

Size and material parameters

Appendix 1—table 1. Parameters adopted in this work

Geometry parameters	Normalized radii[1]	R_1=0.7	R_2=0.8	R_2'=0.96	R_3=1
	The location of muscles[2]	$\theta_1 = \frac{2}{3}\pi$ $\theta_2 = \frac{5}{6}\pi$	$\theta_3 = \frac{7}{6}\pi$ $\theta_4 = \frac{4}{3}\pi$	$\theta_5 = \frac{5}{3}\pi$ $\theta_6 = \frac{11}{6}\pi$	$\theta_7 = \frac{1}{6}\pi$ $\theta_8 = \frac{1}{3}\pi$
Material parameters (Shear modulus)[3]	Actin part	$\mu_a = 5$			
	Epidermis part	$\mu_e = 1$			
	Muscles	$\mu_m = 100$			
	Soft inner part	$\mu_i = 1/200$			

[1] The radii are extracted or inferred from the Ref.(***Ben Amar et al.*** (***2018***); ***Lardennois et al.*** (***2019***)).
[2] The position and size of the muscles are inferred from the Ref.(***Moerman and Williams*** (***2006***); ***Lardennois et al.*** (***2019***)).
[3] The units of the shear modulus are the KPa and is scaled by the epidermis one. It gives for the muscle, a value consistent with the muscle shear modulus proposed in (***Denham et al.*** (***2018***)).

Appendix 2

Analytical model of the early elongation

The finite deformation gradient: $\mathbf{F}_0 = Diag(r'(R), r(R)/R, \lambda)$, and $\mathbf{G}_0 = Diag(1, g_0, 1)$, $0 < g_0 < 1$ in the actin layer, and $g_0 = 1$ in the part without actin bundles. To determine the finite strain $\mathbf{G}_0$, we converted the four muscle parts into thin layers attached to the epidermis in equal proportions to ensure the continuity of the model, and divided our model into four parts, see Fig.1. The actin layer($R_3 < R < R_2'$), epidermis layer($R_2 < R < R_2'$) and muscle layer($R_1' < R < R_2$) are considered as incompressible materials, and the inner part($0 < R < R_1'$) is compressible. The Neo-Hookean energy function is used for the incompressible parts:

$$W = \mu \left[\frac{1}{2} \left(Tr \left(\mathbf{F_e} \mathbf{F_e}^T \right) - 3 \right) - q \left(\det \mathbf{F_e} - 1 \right) \right], \tag{19}$$

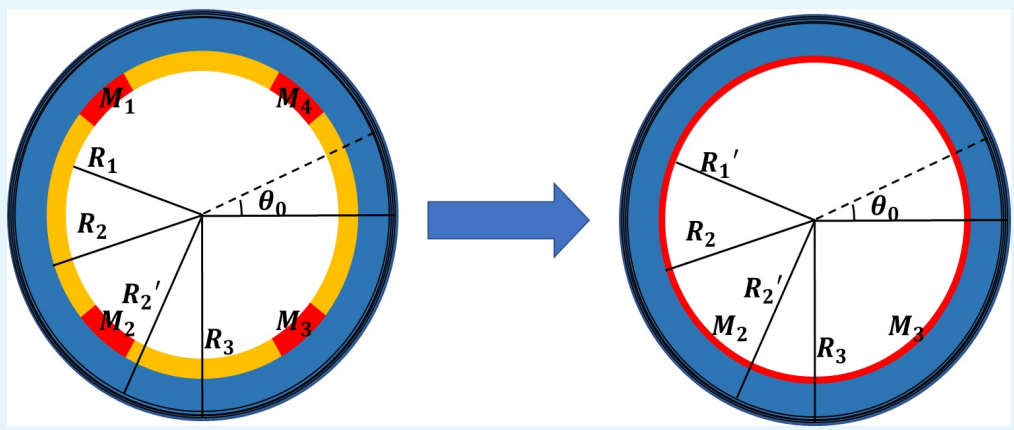

Appendix 2—figure 1. Simplified ross-sectional model with four scattered muscle sections simplified to thin layers ($R_1 = 0.7$, $R_1' = 0.768$, $R_2 = 0.7$, $R_2' = 0.96$).

According to the Euler-Lagrange equations, we can obtain the radius of the actin layer(r_a), the epidermis layer(r_e), and the muscle layer(r_m):

$$r_a = \sqrt{\frac{g_0 R^2 + A}{\lambda}}, \quad r_e = \sqrt{\frac{R^2 + E}{\lambda}}, \quad r_m = \sqrt{\frac{R^2 + M}{\lambda}}. \tag{20}$$

where A, E and M are constants, and the Lagrange multiplier q in the actin, epidermis and muscle layers:

$$q_a = \frac{-\log(R) + \frac{1}{2} g_0{}^2 \left(-\frac{A}{A + g_0 R^2} + \log\left(A + g_0 R^2\right) \right)}{g_0 \lambda} + C_a, \tag{21}$$

$$q_e = -\frac{\frac{E}{E+R^2} + 2\log(R) - \log\left(E + R^2\right)}{2\lambda} + C_e, \tag{22}$$

$$q_m = -\frac{\frac{M}{M+R^2} + 2\log(R) - \log\left(M + R^2\right)}{2\lambda} + C_m. \tag{23}$$

For the compressible part, we take the energy function form (***Holzapfel*** (***2000***)):

$$W = \frac{\mu}{2} \left(Tr \left(\mathbf{F_e} \mathbf{F_e}^T \right) - 3 + \kappa \left(\det \mathbf{F_e} - 1 \right)^2 \right) \tag{24}$$

where κ is a material constant. The radius of the inner part is:

$$r_i = \frac{aR}{\sqrt{\lambda}} \tag{25}$$

where a is a constant.

By considering the boundary condition $\sigma_{rr} = 0$ on the outer border $R = 1$:

$$\sigma_{arr}(R = 1) = \mu_a \left[\left(\frac{\partial r_a(1)}{\partial R} \right)^2 - q_a(1) \right] = 0 \tag{26}$$

the continuity of the radius:

$$r_a(\mathrm{R}_2{}') = r_e(\mathrm{R}_2{}'), \quad r_e(\mathrm{R}_2) = r_m(\mathrm{R}_2), \quad r_m(\mathrm{R}_1{}') = r_i(\mathrm{R}_1{}'), \tag{27}$$

and the continuity of the radial stresses σ_{rr} in $R_2{}'$ and R_2 :

$$\mu_a \left[\left(\frac{\partial r_a(\mathrm{R}_2{}')}{\partial R} \right)^2 - q_a(\mathrm{R}_2{}') \right] = \mu_e \left[\left(\frac{\partial r_e(\mathrm{R}_2{}')}{\partial R} \right)^2 - q_e(\mathrm{R}_2{}') \right], \tag{28}$$

$$\mu_e \left[\left(\frac{\partial r_e(\mathrm{R}_2)}{\partial R} \right)^2 - q_e(\mathrm{R}_2) \right] = \mu_m \left[\left(\frac{\partial r_m(\mathrm{R}_2)}{\partial R} \right)^2 - q_m(\mathrm{R}_2) \right]. \tag{29}$$

Using the above equations, we can obtain expressions for the constants E, M, C_a, C_e and C_m.

We replace all size and material parameters and $\kappa = 100$, $\lambda = 1.8$ in the last condition $\sigma_{mrr}(\mathrm{R}_1{}') = \sigma_{irr}(\mathrm{R}_1{}')$:

$$\mu_m \left[\left(\frac{\partial r_m(\mathrm{R}_1{}')}{\partial R} \right)^2 - q_m(\mathrm{R}_1{}') \right] = \mu_i \sigma_{irr}(\mathrm{R}_1{}'), \tag{30}$$

where σ_{irr}:

$$\sigma_{irr} = \frac{2}{\det \mathbf{F_e}} \left((\det \mathbf{F_e})^2 \frac{\partial W}{\partial (\det \mathbf{F_e})^2} + \frac{\partial W}{\partial (tr(\mathbf{F_e}\mathbf{F_e}^T))} r_i{}'(R)^2 \right). \tag{31}$$

and obtain the relation with constant A and g_0.

Finally, by prescribing a zero traction condition on the top of the cylinder, the muscle part was noticeably considered inextensible, so there was no stress on the top:

$$\int_{R_2{}'}^{1} \sigma_{azz} r_a r_a{}' dR + \int_{R_2}^{R_2{}'} \sigma_{ezz} r_e r_e{}' dR + \int_{0}^{R_1{}'} \sigma_{izz} r_i r_i{}' dR, \tag{32}$$

where:

$$\sigma_{azz} = \lambda^2 - q_a, \quad \sigma_{ezz} = \lambda^2 - q_e, \tag{33}$$

$$\sigma_{izz} = \frac{2}{\det \mathbf{F_e}} \left((\det \mathbf{F_e})^2 \frac{\partial W}{\partial (\det \mathbf{F_e})^2} + \frac{\partial W}{\partial (tr(\mathbf{F_e}\mathbf{F_e}^T))} \lambda^2 \right), \tag{34}$$

all solutions $g_0 = 0.88$, $A = 0.08$ and $r_a(1) = 0.73$ can be determined. The result is also in good agreement with the experimental data (***Vuong-Brender et al.*** (***2017a***); ***Ben Amar et al.*** (***2018***)).

Appendix 3

Time-scale for myosin detachment

The time required for non-muscle myosin detachment is estimated to be $\tau_0 = 10s$ for free actomyosin filaments. If the actin filament is subjected to an external load perpendicular to its axis, detachment can be facilitated, or on the contrary, inhibited, see (***Howard and Clark*** (***2002***)), page 169-170. In the present case, the stresses acting in the radial direction of an actin bundle are compressive and thus will retard the detachment. This energy must be compared to the energy of detachment of all myosin motors from the bundle. The corresponding elastic energy associated with the radial deformation for an actin cable of length l_a with radius $r_b = 0.05\mu m$ estimated from (***Lardennois et al.*** (***2019***)) and shear modulus $\mu_a = 5\ KPa$ is given by $1/2\mu_a(1 - g_0(t))\pi l_a r_b^2 = 210^{-11} l_a\ J$. This result must be compared to the individual energy of detachment times the number of myosin motors on a cable. This number is difficult to determine but an estimate is given by the length of the cable l_a divided by the distance between 2 myosin anchoring sites, which is about $5nm$ while the attachment energy per motor is about $6k_bT$. These values are for skeletal muscle myosins (***Howard and Clark*** (***2002***)) and must be taken with caution. Nevertheless, the order of magnitude of the detachment energy for a collection of myosin heads from actin cable can be estimated to be $4.8 l_a 10^{-12} J$. Then the ratio between the two quantities is of the order $4(1 - g_0(t))$, which explains that the time scale of debonding for a cable under compressive stress in the direction orthogonal of its axis is then:

$$\tau_{deb} = \tau_0 e^{p_3(1-g_0(t))} \tag{35}$$

where p_3 is a positive constant of order one that cannot be predicted exactly. This time scale justifies the exponential correction in Eq.(3) of the manuscript.

Appendix 4

Modelling in the absence of pre-strain

The paper discusses the case with pre-strain. Here, are more details about the case without pre-strain ($\mathbf{G_0} = \mathbf{I}$). Up to the lowest order, the solution of the Euler–Lagrange equations is obviously given by $\mathbf{a}^{(0)} = (R, \Theta, 0)$, and $p^{(0)} = 1$, so there is no deformation and the zero and first order energies vanish. At order $\mathcal{O}\left(\varepsilon^2\right)$ of the elastic energy, the solutions for the active strain components are

$$\begin{aligned} a_1^{(1)} &= -\frac{R}{2}\xi - \frac{R^2}{8}\left(u_1 \sin\Theta - u_2 \cos\Theta\right) + f_1(R), \\ a_2^{(1)} &= \frac{5R}{8}\left(u_1 \cos\Theta + u_2 \sin\Theta\right) + f_2(R), \\ a_3^{(1)} &= 0, \\ p^{(1)} &= f_3(R). \end{aligned} \tag{36}$$

where $f_{1,2}$ are functions related to the active stress g and the fiber angles α and β:

$$\begin{aligned} f_1(R) &= \frac{gR}{2}, \\ f_2(R) &= glog(R)\sin^2\alpha \sin(2\beta), \\ f_3(R) &= 2g\mu log(R)\sin^2\alpha \sin(2\beta). \end{aligned} \tag{37}$$

The stiffness coefficients :

$$\begin{aligned} A_2 &= \frac{9\mu R}{8}, \\ B_2 &= \frac{81}{128}\mu R^3 \sin^2\Theta, \\ C_2 &= \frac{81}{128}\mu R^3 \cos^2\Theta, \\ D_2 &= \frac{\mu R^3}{2}. \end{aligned} \tag{38}$$

The deformation coefficients :

$$\begin{aligned} A_1 &= -\frac{1}{8}g\mu R\left[4 + 5\cos(2\alpha) + 2\cos(2\beta)(-1 + 2\log(R))\sin^2\alpha\right], \\ B_1 &= -\frac{1}{16}g\mu R^2\left[10 + 17\cos(2\alpha) + 2\cos(2\beta)(-1 + 14\log(R))\sin^2\alpha\right]\sin\Theta, \\ C_1 &= \frac{1}{16}g\mu R^2\left[10 + 17\cos(2\alpha) + 2\cos(2\beta)(-1 + 14\log(R))\sin^2\alpha\right]\cos\Theta, \\ D_1 &= -g\mu R^2 \cos\beta \sin(2\alpha). \end{aligned} \tag{39}$$

Modelling with pre-strain

The first-order solutions of the theory with the case of pre-strain, $h_{1,2,3}(R)$, are related to the activation g and the fiber angles α and β:

$$\begin{aligned} h_1(R) &= \frac{R(c+g)}{2\sqrt{\lambda}}, \\ h_2(R) &= g\log(R)\sin^2\alpha \sin(2\beta), \\ h_3(R) &= \frac{2\mu log(R)\left[c + g\cos(2\beta)\sin^2\alpha\right]}{\lambda}. \end{aligned} \tag{40}$$

The stiffness coefficients are:

$$
\begin{aligned}
A_2 &= (0.278 + 1.689\mu)\, R, \\
B_2 &= 1.294 R^3 \left[-0.405 + 2.389\mu + (-0.176 + \mu)\cos(2\Theta)\right], \\
C_2 &= -1.294 R^3 \left[0.405 - 2.389\mu + (-0.176 + \mu)\cos(2\Theta)\right], \\
D_2 &= 0.9\mu R^3.
\end{aligned}
\tag{41}
$$

The deformation coefficients are:

$$
\begin{aligned}
A_1 &= \mu R \Big[0.417c - 0.139g - 6.48g\cos^2\alpha - 0.556c\log(R) \\
&\quad + g\left(0.556\cos^2\beta - 0.556\cos(2\beta)\log(R)\right)\sin^2\alpha\Big]. \\
B_1 &= R^2 \Big\{g(-0.828 + 4.830\mu)\cos\beta\log(R)\sin^2\alpha\sin\beta\cos\Theta + 0.198c\sin\Theta \\
&\quad + \Big[0.198g + 0.910c\mu + 1.307g\mu - 4.830g\mu\cos^2\alpha - 1.225c\mu\log(R) \\
&\quad + g\mu\left(-0.397\cos^2\beta - 1.225\cos(2\beta)\log(R)\right)\sin^2\alpha\Big]\sin\Theta\Big\}. \\
C_1 &= R^2 \Big\{g(-0.828 + 4.830\mu)\cos\beta\log(R)\sin^2\alpha\sin\beta\sin\Theta - 0.198c\cos\Theta \\
&\quad + \Big[-0.198g - 0.910c\mu - 1.307g\mu + 4.830g\mu\cos^2\alpha + 1.225c\mu\log(R) \\
&\quad + g\mu\left(0.397\cos^2\beta + 1.225\cos(2\beta)\log(R)\right)\sin^2\alpha\Big]\cos\Theta\Big\}. \\
D_1 &= -g\mu R^2\cos\beta\sin(2\alpha).
\end{aligned}
\tag{42}
$$

Appendix 5

Energy transformation calculations

The energy transformation process is depicted in Fig.1.

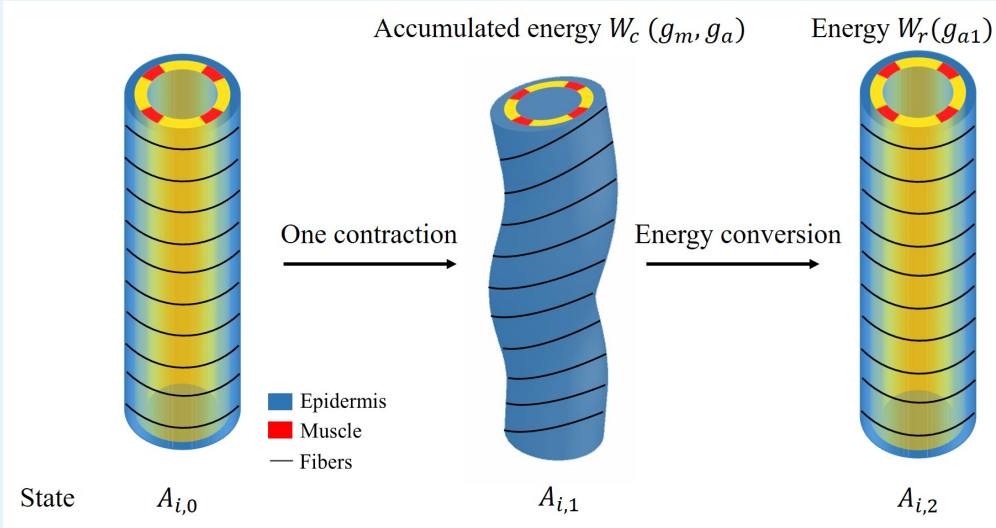

Appendix 5—figure 1. Schematic diagram of energy conversion.

To obtain the elongation $\delta\zeta_i$ after each muscle contraction, we need to calculate the energy, and the total energy has the following form:

$$\mathcal{E} = \varepsilon^2 \int_0^L \mathrm{d}Z \int_S \left(V_0 + \varepsilon V_1 + \varepsilon^2 V_2\right) R\, \mathrm{d}R\, \mathrm{d}\Theta + O\left(\varepsilon^5\right) \tag{43}$$

where the integration domain S refers to each part of the cylinder with a different shear modulus μ, so the model must be divided into 3 different parts for integration.

The final part is the energy conversion per unit volume:

$$\mathcal{E}_{\oint} = \int_S \left(\varepsilon V_1 + \varepsilon^2 V_2\right) R\, \mathrm{d}R\, \mathrm{d}\Theta \tag{44}$$

where V_1 is not the total first-order energy, we consider only the energy induced by the activation of actomyosin g_a and muscle g_m. After obtaining solutions $\mathbf{a}^{(0)}$,$\mathbf{a}^{(1)}$ and deformations from Eq.(11)-(12), the accumulated energy during the contraction period W_c, which we define, is:

$$\begin{aligned} W_c &= \int_S \left(\varepsilon V_1 + \varepsilon^2 V_2\right) R\, \mathrm{d}R\, \mathrm{d}\Theta \\ &= \varepsilon\left(-10.70 g_a - 7.73 g_m\right) + \varepsilon^2\left[\left(-3.31 + 26.75 g_a\right) g_a + 11.95 {g_m}^2\right]. \end{aligned} \tag{45}$$

When the muscles are relaxed and only actomyosin is activated, the total increase in volumetric energy is W_r:

$$\begin{aligned} W_r &= \int_S \left(\varepsilon V_1 + \varepsilon^2 V_2\right) R\, \mathrm{d}R\, \mathrm{d}\Theta \\ &= -0.41 \varepsilon g_{a1} + \varepsilon^2\left(-5.19 + 6.96 g_{a1}\right) g_{a1}. \end{aligned} \tag{46}$$

By calculating the energy conversion, we obtain $g_{a1} = -0.66$ at the beginning of the late elongation phase, Fig.7 of the manuscript shows the elongation for each contraction and total elongation varies with time.